nanomaterials

MDPI

Article

Comparative Study of α- and β-MnO_2 on Methyl Mercaptan Decomposition: The Role of Oxygen Vacancies

Hong Su [1,2], Jiangping Liu [1,2,*], Yanan Hu [1,2], Tianhao Ai [1,2], Chenhao Gong [1,2], Jichang Lu [1,2,*] and Yongming Luo [2,3]

[1] Faculty of Environmental Science and Engineering, Kunming University of Science and Technology, Kunming 650500, China
[2] The Innovation Team for Volatile Organic Compounds Pollutants Control and Resource Utilization of Yunnan Province, The Higher Educational Key Laboratory for Odorous Volatile Organic Compounds Pollutants Control of Yunnan Province, Kunming 650500, China
[3] Faculty of Chemical Engineering, Kunming University of Science and Technology, Kunming 650500, China
* Correspondence: liujiangping@kust.edu.cn (J.L.); lujichangc7@kust.edu.cn (J.L.); Tel./Fax: +86-871-65103845 (Jiangping Liu)

Abstract: As a representative sulfur-containing volatile organic compounds (S-VOCs), CH_3SH has attracted widespread attention due to its adverse environmental and health risks. The performance of Mn-based catalysts and the effect of their crystal structure on the CH_3SH catalytic reaction have yet to be systematically investigated. In this paper, two different crystalline phases of tunneled MnO_2 (α-MnO_2 and β-MnO_2) with the similar nanorod morphology were used to remove CH_3SH, and their physicochemical properties were comprehensively studied using high-resolution transmission electron microscope (HRTEM) and electron paramagnetic resonance (EPR), H_2-TPR, O_2-TPD, Raman, and X-ray photoelectron spectroscopy (XPS) analysis. For the first time, we report that the specific reaction rate for α-MnO_2 (0.029 mol g^{-1} h^{-1}) was approximately 4.1 times higher than that of β-MnO_2 (0.007 mol g^{-1} h^{-1}). The as-synthesized α-MnO_2 exhibited higher CH_3SH catalytic activity towards CH_3SH than that of β-MnO_2, which can be ascribed to the additional oxygen vacancies, stronger surface oxygen migration ability, and better redox properties from α-MnO_2. The oxygen vacancies on the catalyst surface provided the main active sites for the chemisorption of CH_3SH, and the subsequent electron transfer led to the decomposition of CH_3SH. The lattice oxygen on catalysts could be released during the reaction and thus participated in the further oxidation of sulfur-containing species. CH_3SSCH_3, S^0, SO_3^{2-}, and SO_4^{2-} were identified as the main products of CH_3SH conversion. This work offers a new understanding of the interface interaction mechanism between Mn-based catalysts and S-VOCs.

Keywords: CH_3SH decomposition; MnO_2; oxygen vacancies; oxygen migration

check for updates

Citation: Su, H.; Liu, J.; Hu, Y.; Ai, T.; Gong, C.; Lu, J.; Luo, Y. Comparative Study of α- and β-MnO_2 on Methyl Mercaptan Decomposition: The Role of Oxygen Vacancies. *Nanomaterials* **2023**, *13*, 775. https://doi.org/10.3390/nano13040775

Academic Editor: Antonio Guerrero-Ruiz

Received: 24 January 2023
Revised: 5 February 2023
Accepted: 15 February 2023
Published: 19 February 2023

1. Introduction

As a particular class of volatile organic compounds (VOCs), sulfur-containing volatile organic compounds (S-VOCs) can be converted into sulfate aerosols in the atmosphere through complex physicochemical reactions [1]. They can also react indirectly with NO_x through photochemistry reactions, which are the crucial precursors for forming $PM_{2.5}$ and O_3. Methyl mercaptan (CH_3SH), a representative S-VOC, is considered as an important air odor pollutant, which is harmful to the ecosystem and human health owing to its severe toxicity and low olfactory threshold [2–4]. In previous studies, various methods have been employed to eliminate CH_3SH, such as adsorption [5,6], biodegradation [7], photocatalytic oxidation [8], and catalytic oxidation [9,10]. However, these remediation technologies suffer from secondary pollution because of incomplete removal and high cost. Until now, catalytic decomposition has been regarded as the most promising strategy for removing S-VOCs

due to its high purification efficiency, energy-saving nature, lack of additional additives (O_2, H_2, O_3, etc.), and less secondary pollution [11,12].

Metal-based catalysts are widely used for the removal of VOCs on account of their superior catalytic performance. Among the various transition metal oxides, MnO_2 is of great interest because of its low cost, low toxicity, environmental friendliness, and wide natural distribution [13,14]. Meanwhile, MnO_2 has been extensively studied in heterogeneous catalysis due to its unique physicochemical properties (i.e., multivalent, reactive oxygen species, and polycrystalline nature) and is recognized as one of the most active catalysts for VOCs removal among transition metal oxides [15–17]. Nanostructured MnO_2 possesses a rich structural flexibility, which adopts various crystallographic forms such as α-, β-, δ-, and γ-MnO_2, depending upon the size of the tunnel [18,19]. These polymorphs of MnO_2 include a one-dimensional chain-like tunnel (α-, β-, and γ-MnO_2) and two-dimensional layer structures (δ-MnO_2) based on different linkage ways of the basic octahedral molecular sieves [20,21].

Among the MnO_2 polymorphs, α-MnO_2 has one of the largest tunnel sizes (4.6 Å) consisting of 1D (1 × 1) and (2 × 2) channels, composed of double chains of edge-sharing [MnO_6] octahedra, filled with alkali metal cations, NH_4^+ or H_3O^+, inside the 2 × 2 tunnels to stabilize the structure [16]. The pyrolusite-type β-MnO_2 has a rutile-type structure with infinite [MnO_6] octahedral chains that share opposing edges. Each chain is connected to four similar chain corners, forming the smallest tunnel structure (2.3 Å) of MnO_2 polymorphs, consisting of 1D (1 × 1) and (1 × 1) channels [22,23]. It is generally accepted that catalysts with different crystal structures exhibit different catalytic efficiencies and reaction mechanisms for the reactants. For instance, Hayashi et al. evaluated the aerobic catalytic performance of six types of MnO_2 (α-, β-, γ-, δ, λ, ε -phases) for the transformation of 5-hydroxymethylfurfural to 2,5-furandicarboxylic acid and concluded the best activity of β-MnO_2 [19]. Chen et al. found that the α- and γ-MnO_2 presented higher benzene oxidation activity than β- and δ-MnO_2, whereas δ-MnO_2 displayed the best in formaldehyde oxidation among all of the MnO_2 materials [20]. This may be due to the varying oxygen species in different types of MnO_2, which play distinct roles in the catalytic oxidation of formaldehyde and benzene. In addition, surface defects of manganese-based catalysts are regarded as an important determinant of their catalytic activity, and their formation and driving of catalytic reactions are often related to their surface oxygen species [24–26]. Yang et al. investigated the phase-activity relationship of MnO_2 toward toluene catalytic oxidation. They proposed that the excellent catalytic performance of δ-MnO_2 may be associated with the rich oxygen vacancy and the strong mobility of oxygen species [27]. Tian et al. prepared α-, β-, and ε- MnO_2 for CO oxidation and found that β-MnO_2 possesses the lowest energies for oxygen vacancy generation as well as excellent redox properties, thus exhibiting the best CO oxidation activity [13]. These studies highlight the importance of oxygen vacancies in VOC removal and illustrate that the concentration of oxygen vacancies in different crystal structures tends to dominate their catalytic activity. Therefore, it is necessary to understand the relationship between the catalytic activity of manganese oxide and its surface structure to provide a standard for the further modification of MnOx or other metal oxide catalysts. However, noticeable differences are presented in the surface morphology and crystal structure of different crystalline MnO_2, which makes it difficult to clarify the contribution of oxygen vacancies to the catalytic reaction. For example, δ-MnO_2 is a layered structure, whereas α-, β- and γ-MnO_2 are common tunneling structures. Among them, γ-MnO_2 is a spherical structure, and α- and β-MnO_2 are similar nanorod-like structures. The differences in crystal structure and surface morphology can inherently lead to variations in catalyst surface properties, which can obscure the critical role of oxygen vacancies. Therefore, it is essential to reveal the effect of surface vacancies on catalytic reactions based on the same morphology. In addition, oxygen vacancy-mediated catalytic reactions may be accompanied by the migration and release of oxygen species and the generation of new oxygen vacancies, thus the transformation of these active surface species in catalytic reactions and their contribution to the removal of VOCs need further clarification.

Herein, we compared the removal efficiency of CH_3SH by α-MnO_2 and β-MnO_2 with similar surface morphology but different crystal structures. Their physicochemical properties were subsequently characterized by various analysis techniques. The number of surface low valence Mn, oxygen vacancies and redox properties were studied regarding high-resolution transmission electron microscope (HRTEM) and electron paramagnetic resonance (EPR), X-ray photoelectron spectroscopy (XPS), H_2-TPR and O_2-TPD. The changes of catalyst surface species before and after the reaction were characterized by XPS, and the variation of intermediate species of CH_3SH during the reaction were also monitored.

2. Materials and Methods

2.1. Chemical Reagents

α-MnO_2 and β-MnO_2 were synthesized through the hydrothermal synthesis method according to previous research [28]. Potassium permanganate ($KMnO_4$, Chengdu Colon Chemicals Co., LTD, Chengdu, China), hydrated manganese sulfate ($MnSO_4 \cdot H_2O$, Aladdin Reagent Co., LTD, Shanghai, China) and ammonium persulfate ($(NH_4)_2S_2O_8$, Aladdin Reagent Co., LTD, Shanghai, China) were used without further purification.

Synthesis of α-MnO_2: 0.1 M $KMnO_4$ and 0.05 M $MnSO_4 \cdot H_2O$ were dissolved in 70 mL deionized water and stirred for 30 min. The resulting solution was transferred to a 100 mL Teflon-lined autoclave and maintained at 160 °C for 12 h. After cooling to room temperature, the precipitate was centrifuged and washed with distilled water (700–1000 mL) three times. Finally, the precipitate was dried at 80 °C for 4 h and calcination at 360 °C for 2 h.

Synthesis of β-MnO_2: 0.14 M $MnSO_4 \cdot H_2O$ and 0.14 M $(NH_4)_2S_2O_8$ were dissolved in 70 mL deionized water and stirred for 30 min. The resulting solution was transferred to a 100 mL Teflon-lined autoclave and maintained at 140 °C for 12 h. After cooling to room temperature, the precipitate was centrifuged and washed with distilled water (700–1000 mL) three times. Finally, the precipitate was dried at 80 °C for 4 h and calcination at 360 °C for 2 h.

2.2. Catalyst Characterization

The refined test of X-ray powder diffraction (XRD) of the products was performed using a Bragg-Brentano-type powder diffractometer (Nihongo TTRIII, Tokyo City, Japan, operated at 40 kV and 200 mA, Cu Kα radiation, λ = 0.15418 nm). To investigate the Brunauer-Emmett-Teller (BET) surface areas, average pore diameters, and total pore volumes of the samples, N_2 adsorption-desorption isotherms were determined using a NOVA 4200e Surface Area and Pore Size Analyzer. Electron paramagnetic resonance (EPR) signals were carried out on a Bruker A300 spectrometer (Saarbrucken, Germany) at 25 °C. XPS profiles were obtained with a Thermo Scientific K-Alpha spectrometer (Waltham, MA, USA). The binding energy (BE) values were calibrated using the C 1 s peak at 284.8 eV. The Raman spectra were recorded using a 514 nm laser excitation source with an integration time of 3 s and 30 accumulations (Raman, BX41, HOEIBA Scientific, Paris, France). Scanning electron microscopy (SEM, VEGA3SBH, Brno, Czech Republic) and high-resolution transmission electron microscopy (HRTEM, Talos F200X, Thermo Scientific, Waltham, MA, USA) were used to observe catalyst morphologies.

Hydrogen temperature-programmed reduction (H_2-TPR) and oxygen temperature-programmed desorption (O_2-TPD) experiments were performed on a FULI II 7970 gas chromatograph (Fuli Analytical Instrument Inc., Hangzhou, China) with a thermal conductivity detector (TCD). In H_2-TPR experiments, 50 mg of the sample was placed in a quartz tube and pretreated in a gas flow of 10% H_2/Ar (30 mL min^{-1}) at 100 °C for 30 min to remove impurities. After the pretreatment process, the sample was reduced by 10% H_2/Ar (30 mL min^{-1}) from 100 to 800 °C with a heating rate of 10 °C/min. For O_2-TPD analysis, 50 mg of sample was loaded on the quartz tube, heated to 105 °C and pretreated with He (30 mL min^{-1}) for 30 min to remove surface adsorbed water, followed by cooling to 30 °C. Subsequently, the sample was adsorbed by 10% O_2/He (30 mL min^{-1}) at room temperature for 60 min, and then He (30 mL min^{-1}) was used to purge the sample for

30 min to remove physically adsorbed O_2 and stabilize the baseline. Subsequently, the temperature was ramped from 30 to 850 °C at 10 °C mL min^{-1}.

2.3. Catalyst Activity Evaluation

The catalytic performance for the CH_3SH decomposition was investigated in a fixed-bed quartz tube reactor (i.d. = 6 mm). 200 mg samples with the size of 40–60 meshes were loaded into the reactor. The reaction temperature was controlled and maintained for about 1 h at each designated temperature. The inlet CH_3SH concentration was set at 5000 ppm, and the total flow rate was maintained at 30 mL min^{-1}. The concentration of CH_3SH was recorded by GC-9790 (FULI, China) equipped with a flame ionization detector (FID) and flame photometric detector (FPD), and the CH_3SH conversion ratio was calculated as follows:

$$\text{CH}_3\text{SH conversion} = \frac{C_{in} - C_{out}}{C_{in}} \times 100\%$$

C_{in} represents the inlet concentration of CH_3SH and C_{out} is the outlet concentration of CH_3SH.

The reaction rates of CH_3SH decomposition were determined in the kinetic regime at a CH_3SH conversion lower than 20% at different temperatures; The reaction rate (r_{CH3SH}; mol g^{-1} h^{-1}) for CH_3SH decomposition was calculated according to the following equations:

$$r_{CH_3SH} = \frac{C_{CH_3SH} \times X_{CH_3SH} \times F}{m_{cat}}$$

$$r_{norm} = \frac{C_{CH_3SH} \times X_{CH_3SH} \times F}{m_{cat} \times S_{BET}}$$

where the C_{CH_3SH} represents the initial methyl mercaptan concentration, F (mol·h^{-1}) represents the total flow rate, X_{CH_3SH} denotes CH_3SH conversion, and S_{BET} (m^2·g^{-1}) represents the specific surface area of catalysts.

The turnover frequency (TOF, h^{-1}) was calculated for different crystal types based on oxygen vacancy concentration for MnO_2, and indicates the number of reactions of methyl mercaptan at each active site per unit of time, thus TOF was obtained using the following equation:

$$TOF\left(h^{-1}\right) = \frac{C_{CH_3SH} \times X_{CH_3SH} \times F}{\frac{m_{MnO_2}}{M_{MnO_2}} \times (Mn^{2+} + Mn^{3+})}$$

M_{MnO_2} (mol·g^{-1}) is the molar mass of MnO_2, and $Mn^{2+} + Mn^{3+}$ derived from XPS data, which represent the concentration of the oxygen vacancies of MnO_2 deduced from the obtained XPS spectra.

3. Results and Discussion

3.1. Structure and Morphology

XRD was used to determine the crystal structure of the prepared material. The XRD patterns of as-prepared MnO_2 with various crystal types are shown in Figure 1. The diffraction peaks located at ~12.7°, ~18.1°, ~28.8°, and ~37.5° can be assigned to α-MnO_2 (JCPDS card no. 44-0141) (Figure 1A), and the peaks at ~28.7°, ~37.2°, ~42.7° and ~56.4° can be ascribed to β-MnO_2 (JCPDS card no. 24-0735) (Figure 1B) [29]. There was no apparent crystal transformation on these samples after 360 °C calcination. The sharp and strait peaks of β-MnO_2 could indicate its great crystallization and large grain size; α-MnO_2 presented wide bands with relatively lower crystallinity and smaller grain sizes. The above results indicate the successful obtaining of the two kinds of MnO_2 with specific crystal phases.

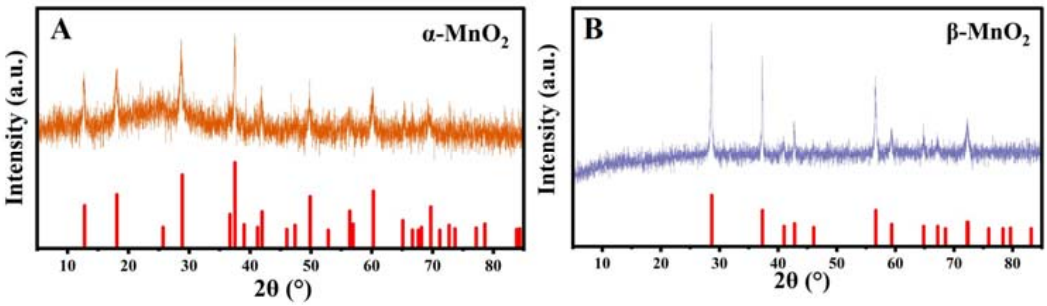

Figure 1. XRD patterns of α-MnO_2 (**A**) and β-MnO_2 (**B**).

The morphologies of MnO_2 samples were characterized by a scanning electron microscopy (SEM), a transmission electron microscope (TEM), and a high-resolution TEM (HRTEM). As can be seen in Figure 2A, α-MnO_2 showed a stacking-nanorod structure with an average length of about 330 nm. β-MnO_2 (Figure 2F) also showed a typical rod shape with a diameter near 50 nm and a length of ~1.2 μm. TEM showed consistent results with the SEM that α-MnO_2 (Figure 2B) and β-MnO_2 (Figure 2G) had similar nanorod-like structures as previously reported [30]. The well-identified periodic lattice fringes of 6.9 Å can be clearly observed in Figure 2C, corresponding to the interplanar distance of (110) facet of α-MnO_2. Figure 2H exhibited the lattice fringes of 3.1 Å, which match the interplanar distance of the (110) facet of β-MnO_2 well. Compared with the β-MnO_2 samples, α-MnO_2 showed more blurry lattice fringes, representing poor crystallinity, which also agrees well with the XRD patterns. In addition, the presence of defects was further demonstrated using the inverse Fast Fourier Transform (FFT) pattern (Figure 2E,J). Significantly more lattice distortion can be clearly observed on the surface of α-MnO_2 (Figure 2D) (highlighted by red ovals), thus leading to more defects than β-MnO_2 [10]. Besides, severe blurring of the lattice fringes was also detected on α-MnO_2 than β-MnO_2. Lattice distortion can be caused by nearby point defects. Simultaneously, a defect layer will be formed once the defect concentration is high enough, resulting in a blurry lattice fringe in the HRTEM images [31]. Hence, the intrinsic defective structure of α-MnO_2 was confirmed. Oxygen vacancies, as an important point defect in catalysts, play a prominent role in the catalytic reaction process, and the high oxygen vacancy concentration will result in a blurry lattice fringe, which can be reflected in the HRTEM images [32]. As shown in Figure 3, the EPR signal corresponding to g = 2.003 can be attributed to oxygen vacancies, and its signal intensity can represent the number of oxygen vacancies [27]. Therefore, more oxygen vacancies on α-MnO_2 than β-MnO_2 can be confirmed based on EPR, consistent with HRTEM analysis.

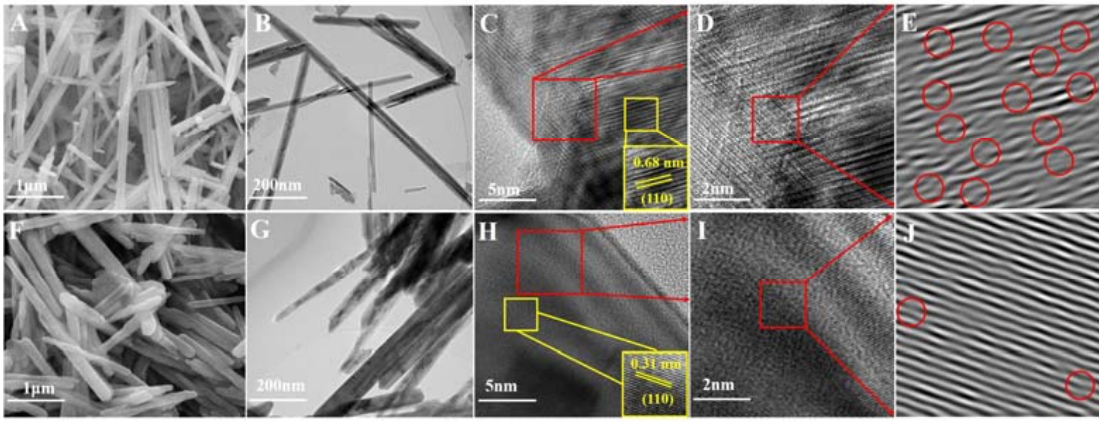

Figure 2. SEM, TEM and HRTEM images of α-MnO_2 (**A**–**D**) and β-MnO_2 (**F**–**I**); The inverse FFT images for α-MnO_2 (**E**) and β-MnO_2 (**J**).

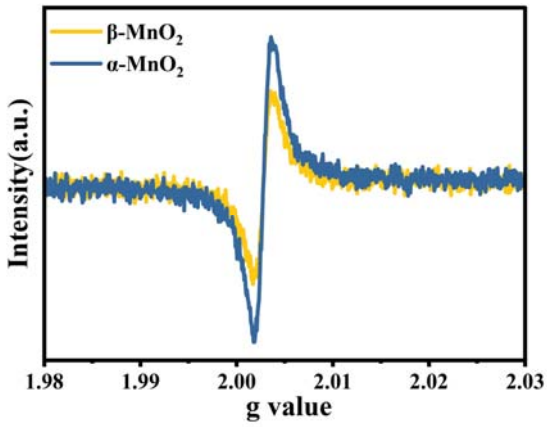

Figure 3. EPR profiles of α-MnO_2 and β-MnO_2.

The BET surface areas (S_{BET}), and pore volumes of the two catalysts are shown in Figure 4A,B. It is reported that the different structures assembled by MnO_6 octahedra in MnO_2 will affect the related surface areas and pore volumes. β-MnO_2 presented relatively low specific surface areas (12.76 m^2 g^{-1}) and pore volumes (0.06 cm^3 g^{-1}), whereas α-MnO_2 showed higher specific surface areas (34.59 m^2 g^{-1}) and pore volumes (0.13 cm^3 g^{-1}). Moreover, the nitrogen adsorption-desorption isotherms of α-MnO_2 and β-MnO_2 displayed a type IV curve with H_3-type hysteresis loops, indicating that both samples were mesoporous structures [33].

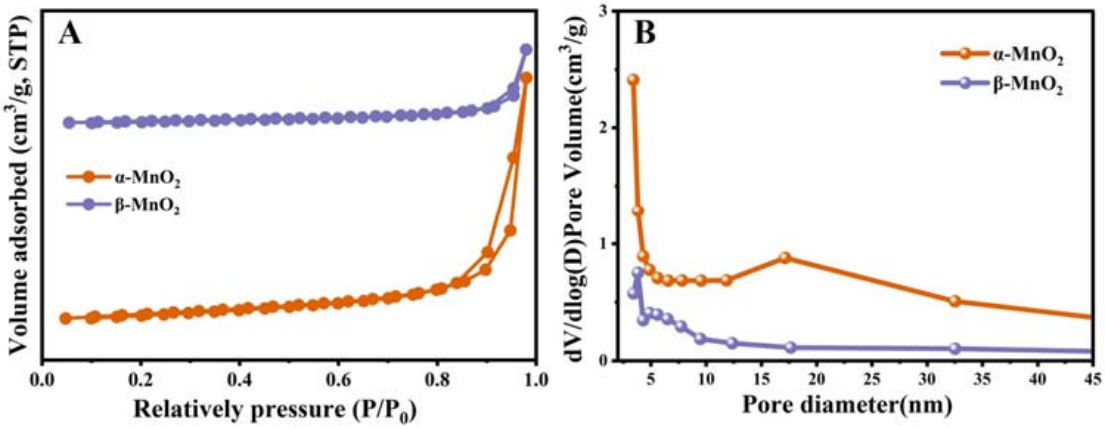

Figure 4. N_2 adsorption-desorption isotherm plots (**A**) and pore distributions (**B**) of α-MnO_2 and β-MnO_2.

3.2. Catalytic Performance

In order to explore the activity of two catalysts on sulfur-containing volatile organic pollutants (S-VOCs), methyl mercaptan (CH_3SH) was chosen as the model S-VOCs, and the catalytic activities of α-MnO_2 and β-MnO_2 are shown in Figure 5A. Two MnO_2 samples exhibited significantly different catalytic performance in CH_3SH catalytic reaction. α-MnO_2 (74%) exhibited significantly better catalyst activity than β-MnO_2 (3%) at 30 °C. The decreases of CH_3SH conversion for α-MnO_2 at 50 °C may be due to the desorption of CH_3SH on the catalyst. As the temperature increased, the conversion of CH_3SH reached 100% at 100 °C with both catalysts. Furthermore, the reaction rates of α-MnO_2 and β-MnO_2 at 50 °C were calculated based on the activity experiments. As shown in Figure 5B, α-MnO_2 showed the CH_3SH reaction rate of 2.9×10^{-2} mol g^{-1} h^{-1}, this being ~4.1 times higher than the rates measured for and β-MnO_2 at 50 °C, which was consistent with the results for the catalytic activity.

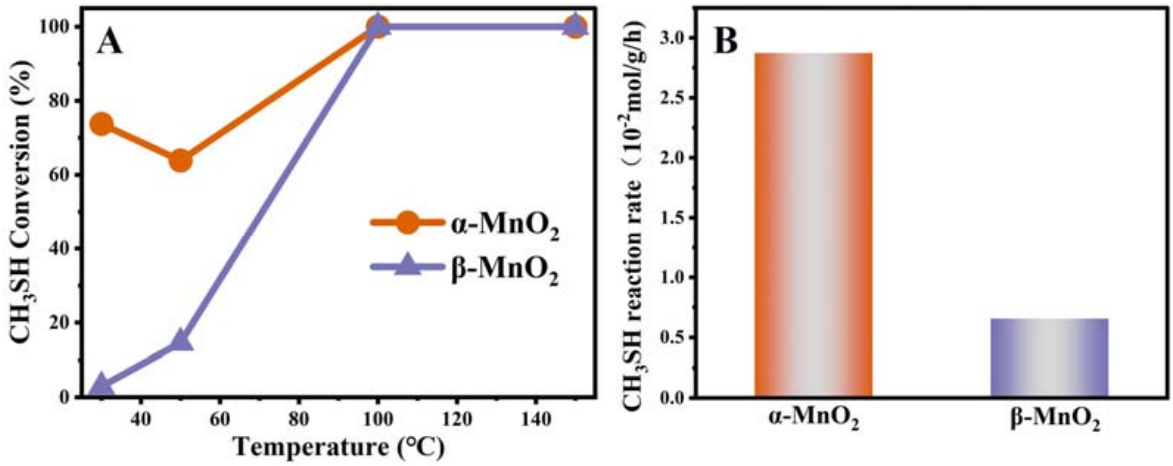

Figure 5. CH_3SH degradation over α-MnO_2 and β-MnO_2 catalysts (**A**). Reaction condition: 0.20 g catalysts, 5000 ppm CH_3SH, total flow rate = 30 mL min^{-1}, WHSV = 9000 mL g^{-1} ·h^{-1}); The reaction rates (×10^{-2} mol g^{-1} h^{-1}) at 50 °C for α-MnO_2 and β-MnO_2 (**B**).

It is well known that the specific surface area plays a critical role in catalytic reactions. To eliminate its influence, the reaction rates with surface area normalization were calculated at different temperatures based on the data from the activity experiments. The results of the normalized reaction rates (r_{norm}, mol m^{-2} h^{-1}) of CH_3SH decomposition are shown in Figure 6A. The normalized reaction rates for α-MnO_2 were obviously higher than those of β-MnO_2 at 30, 50, 60 and 80 °C, which suggested that reactivity was not governed by the specific surface area. Turnover frequency (TOF) is essential for studying the intrinsic reactivity of catalysts. In this work, the TOF (h^{-1}) was calculated based on oxygen vacancy concentration, and the TOF value for the CH_3SH catalytic decomposition was conducted at 50 °C with 0.01 g of catalyst and was calculated within a low CH_3SH conversion (1 h of reaction, below 15.0%). As displayed in Figure 6B, the α-MnO_2 showed the highest TOF value of 0.14 h^{-1}, which was 1.8 times as that of the β-MnO_2 (0.08 h^{-1}), indicating that α-MnO_2 has better catalytic performance for CH_3SH.

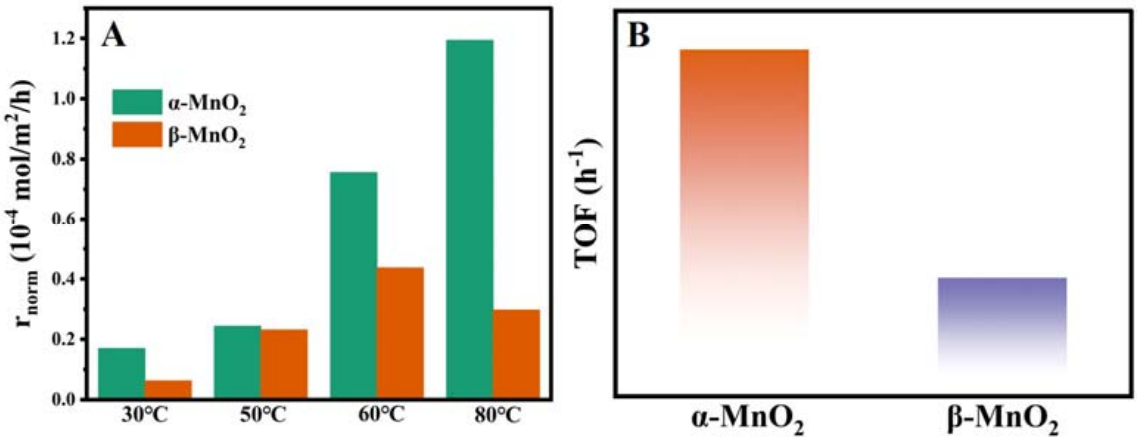

Figure 6. The value of r_{norm} (×10^{-4}, mol·m^{-2} h^{-1}) from 30 to 80 °C for α-MnO_2 and β-MnO_2 (A); The value of TOF (h^{-1}) at 50 °C for α-MnO_2 and β-MnO_2 (B). Reaction conditions: 0.01 g catalysts, 5000 ppm styrene, total flow rate = 30 mL min^{-1}, GHSV = 9000 h^{-1}.

3.3. Redox Capacity and Oxygen Species

To evaluate the reduction behaviors of MnO_2 samples, H_2-temperature-programmed reduction (TPR) was performed (Figure 7A). For α-MnO_2, the peaks at 289 and 309 °C corresponded to the reduction of $Mn^{4+} \rightarrow Mn^{3+}$ and $Mn^{3+} \rightarrow Mn^{2+}$, respectively, and the

peaks around 291 and 317 °C for β-MnO_2 were attributed to $Mn^{4+} \rightarrow Mn^{3+}$ and $Mn^{3+} \rightarrow Mn^{2+}$, respectively [20,34]. The reduction temperature of α-MnO_2 was lower than that of β-MnO_2, indicating that the reduction of α-MnO_2 is relatively faster. More importantly, the more remarkable reduction ability of α-MnO_2 means easier deoxygenation during hydrogen treatment, suggesting that oxygen migration is more likely to occur on its surface. Therefore, α-MnO_2 features stronger oxygen species mobility than β-MnO_2.

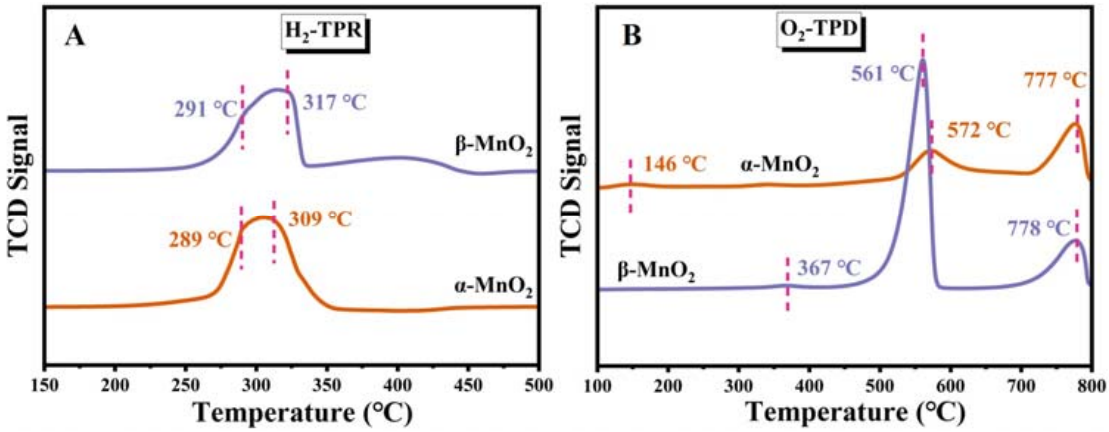

Figure 7. H_2-TPR (**A**) and O_2-TPD (**B**) profiles α-MnO_2 and β-MnO_2.

O_2-TPD was conducted further to explore the oxygen species of the MnO_2 catalysts. Figure 7B shows three desorption peaks related to oxygen species that can be observed on the MnO_2. The low-temperature peak below 400 °C was ascribed to the chemisorbed active oxygen species on the surface (O^- and O_2^-) [35]. The desorption peaks at 400–650 °C and 700–850 °C were related to the release of subsurface and bulk lattice oxygen species (O^{2-}), respectively [36,37]. The desorption of surface oxygen at low temperature (<400 °C) plays the primary role as reactive oxygen species participating in the catalytic reaction [38]. Moreover, the lower temperature of the surface oxygen desorption peak means better low-temperature mobility of oxygen species. As depicted in Figure 7B, α-MnO_2 showed a lower temperature at 146 °C of the surface oxygen desorption peak than β-MnO_2 at 367 °C, indicating the better low-temperature mobility of oxygen species, which is in agreement with H_2-TPR.

More bonding properties were discussed through Raman spectra (Figure 8A). The peaks at 348 and 640 cm^{-1} corresponded to the Mn-O bending and the stretching vibration, respectively [39]. Significantly weaker and broader Raman peaks at around 640 cm^{-1} were detected for α-MnO_2 than β-MnO_2, suggesting lower crystallinity and more defects due to the lattice distortion [40]. To evaluate the strength of the Mn-O bond, the bond force constant (k) was calculated from Hooke's law [41,42] using the following equation: $\omega = \frac{1}{2\Pi c}\sqrt{\frac{k}{\mu}}$, where ω is the Raman shift (cm^{-1}), c is light velocity, and μ is the effective mass of the Mn-O bond. The calculated Mn-O force constant (k) is shown in the inset of Figure 8B. Thus, the Mn-O bond force constant of α-MnO_2 (293 N/m) was smaller than that of β-MnO_2 (296 N/m), implying the weaker Mn-O bond. The weaker Mn-O bond means easier migration of O and easier redox of Mn during the reaction, which is beneficial for catalytic reactions [25].

3.4. Identification of the Role of Oxygen Vacancies in CH_3SH Degradation

The surface elemental composition and chemical state of these MnO_2 samples were identified by XPS. The XPS spectra of Mn $2p_{3/2}$ of the samples are shown in Figure 9. The peaks corresponding to binding energies at 642.7, 641.7 and 640.6 eV can be attributed to Mn^{4+}, Mn^{3+} and Mn^{2+}, respectively [43,44]. It is noteworthy that the binding energy corresponding to different valences of Mn were slightly different in both MnO_2 samples, indicating that crystal phase structure has a certain effect on the electron density of the

MnO_2 surface, which is related to the degree of charge imbalance, oxygen vacancies, as well as the relative content of Mn^{2+}, Mn^{3+} and Mn^{4+} [45]. Specifically, the oxygen vacancy will be generated to maintain electrostatic balance with the increasing Mn^{2+} and Mn^{3+} proportion, and the proportion of low-valence Mn is generally regarded as an indicator of surface oxygen vacancies [44]. As shown in Table 1 and Figure 9A, the proportion of the low valence Mn (Mn^{2+} + Mn^{3+}) showed α-MnO_2 (41.62%) > β-MnO_2 (37.74%). Besides, the average oxidation state (AOS) of MnO_2 was calculated according to the formula of AOS = 8.956 − 1.126 ΔE [46], which was based on the size of Mn 3s multiple splitting (ΔE) in Mn 3s XPS spectra (Figure 10A). The AOS values of the Mn element in α-MnO_2 and β-MnO_2 were calculated to be 3.57 and 3.75, respectively. In previous studies, lower AOS of MnO_2 was also able to indicate more surface oxygen vacancies [47]. Therefore, it can be inferred that α-MnO_2 has a greater surface oxygen vacancy density than β-MnO_2 (in agreement with HETEM and EPR).

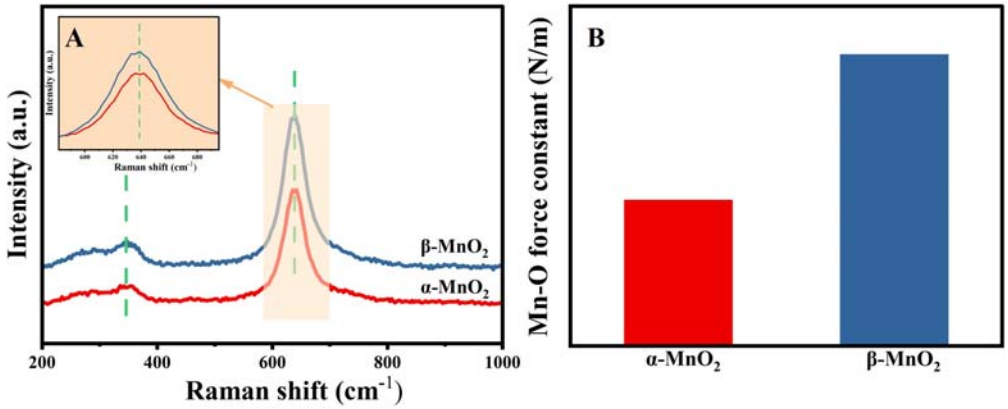

Figure 8. Raman profiles (**A**) and the Mn-O force constant (**B**) of α-MnO_2 and β-MnO_2.

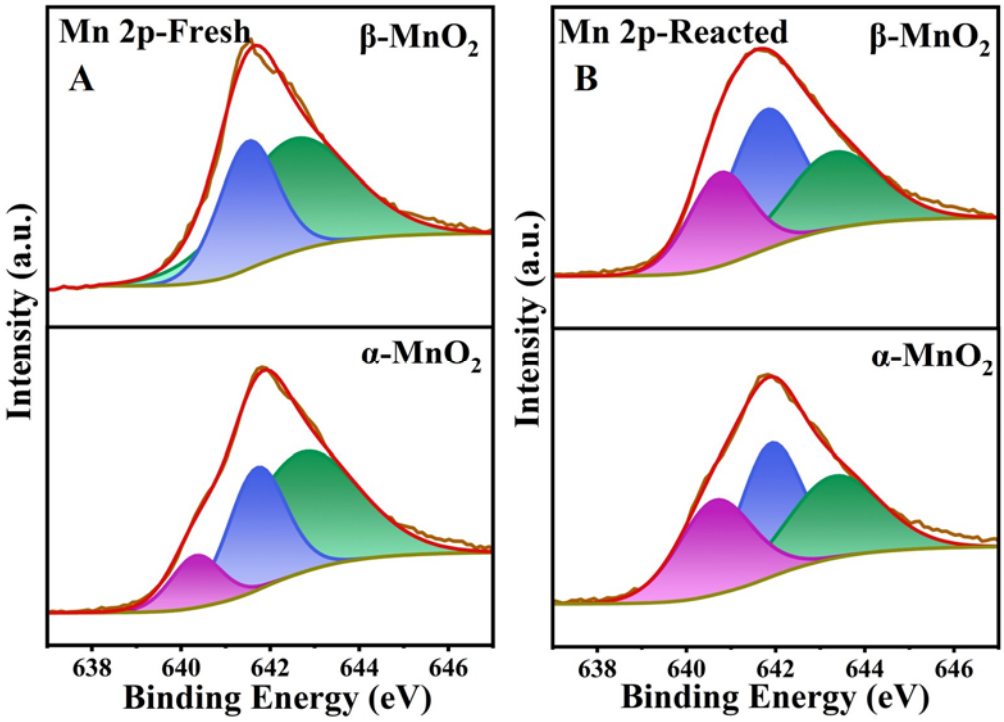

Figure 9. XPS profiles of Mn $2p_{3/2}$ over the fresh (**A**) and spent (**B**) catalysts.

Table 1. Mn 3s Mn $2p_{3/2}$ results before and after the reaction of B-MnO_2 and C-MnO_2.

Catalysts	Mn^{2+} (%)	Mn^{3+} (%)	Mn^{4+} (%)	Mn^{2+} + Mn^{3+}/ Mn^{4+} (%)	AOS [1]
α-MnO_2-Fresh	11.31	30.31	58.38	0.71	3.57
β-MnO_2-Fresh	2.71	35.04	62.26	0.6	3.75
α-MnO_2-Spent	25.19	43.77	31.04	2.22	2.83
β-MnO_2-Spent	16.39	46.99	36.62	1.99	3.25

[1] AOS = 8.956 − 1.126 × ΔE.

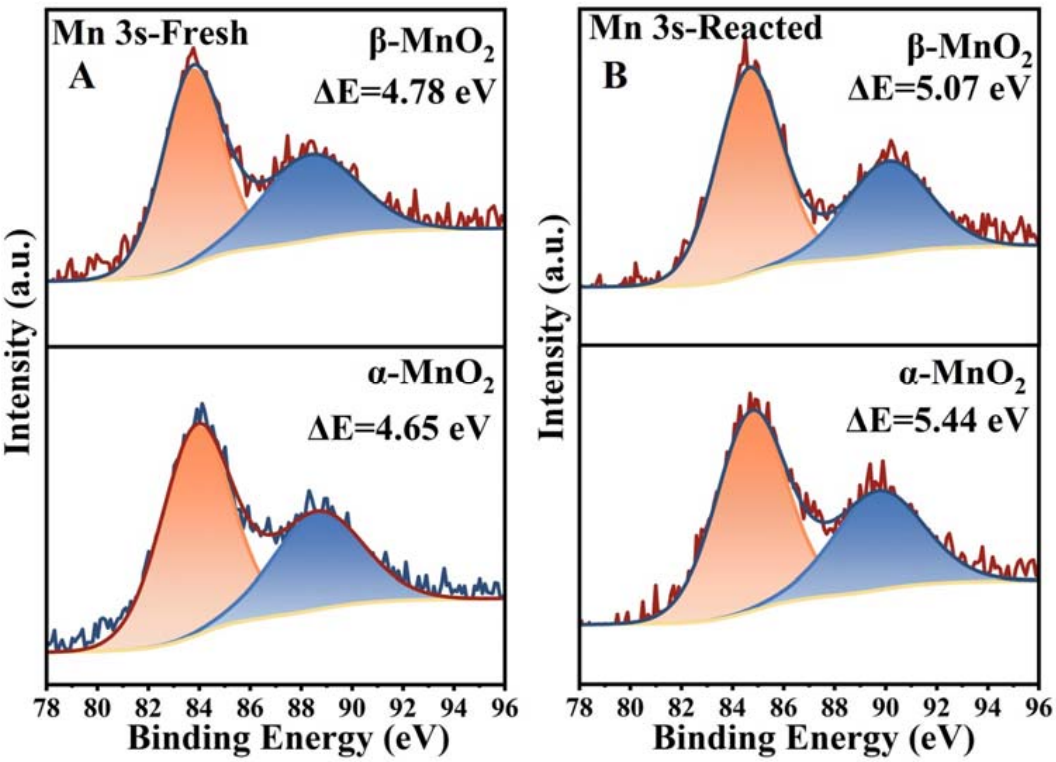

Figure 10. XPS profiles of Mn 3s over the fresh (**A**) and spent (**B**) catalysts.

Additionally, Mn^{2+}-O and Mn^{3+}-O bonds are weaker than Mn^{4+}-O [48]. Thus, the higher ratio of low valence Mn (Mn^{2+} + Mn^{3+}) endows MnO_2 with a larger proportion of weaker M-O bonds on its surface, meaning the easier release of O to participate in the reaction. Figure 9A showed that α-MnO_2 had more low valence Mn (Mn^{2+} + Mn^{3+}) than β-MnO_2, which also implies the easier release of surface oxygen species, consistent with the results of H_2-TPR and O_2-TPD. Comparison of the Mn $2p_{3/2}$ spectra before and after the reaction (Figure 9B) of MnO_2 with CH_3SH showed that the valence state of Mn in both samples changed obviously, suggesting the electron transfer during the reaction. For both samples, Mn^{4+} decreased, and Mn^{2+} and Mn^{3+} increased, proving that the high-valent Mn (IV) was reduced by gaining electrons during the reaction. After the reaction, the Mn^{2+}+Mn^{3+}/Mn^{4+} of α-MnO_2 increased by 1.51 and that of β-MnO_2 by 1.39, and AOS decreased by 0.74 for α-MnO_2 and that of β-MnO_2 decreased by 0.5 (Figure 10B), testifying that α-MnO_2 was reduced to a greater extent by gaining more electrons than β-MnO_2, which can well match H_2-TPR results. It is noteworthy that higher AOS usually indicates a stronger electron-gaining ability of the catalyst because of the presence of more high-valent atoms, however, α-MnO_2 exhibited a stronger electron-gaining ability in the reaction with CH_3SH, suggesting that oxygen vacancies play a more important role in catalyzing CH_3SH comparing to the high-valent Mn. This may explain the fact that chemisorption is the

rate-limiting step for electron transfer, and more surface oxygen vacancies provide more surface adsorption sites for CH_3SH.

In addition, the reaction between CH_3SH and the catalyst could change the electronic environment of the catalyst. During the reaction, as the ratio of Mn^{2+} and Mn^{3+} increased, weaker Mn-O bonds were continuously formed and broken, leading to deoxygenation and further generation of oxygen vacancies to maintain electrostatic equilibrium, which may provide new sites for the reaction, and these desorbed oxygen species may favor the catalytic oxidation of CH_3SH as well.

The XPS spectra of O 1s of the samples are shown in Figure 11. Peaks with binding energies at 529–529.8, 530.9–532 and 533 eV in the XPS spectra of O 1s of the MnO_2 samples (Figure 11) can be attributed to lattice oxygen (O_{latt}) and surface adsorption oxygen (O_{ads}), and surface hydroxyl oxygen ($O_{adsO\text{-}H}$), respectively [49–51]. The molar ratio of O_{ads}/O_{latt} is shown in Table 2 and follows the order of α-MnO_2 (0.65) > β-MnO_2(0.35). O_{ads} was generally considered the most reactive oxygen species in the catalytic reaction and capable of participating in the catalytic oxidation of VOCs in previous reports [52,53]. The oxygen species changes before and after the reaction are shown in Figure 11B and Table 2. The O_{latt} and O_{ads} for both two materials decreased and increased, respectively, suggesting the migration of O_{latt} to form O_{ads} during the reduction of Mn. Obviously, α-MnO_2 formed more O_{ads} after the reaction, which corresponds to its greater degree of reduction, also implying that α-MnO_2 has a stronger catalytic capacity.

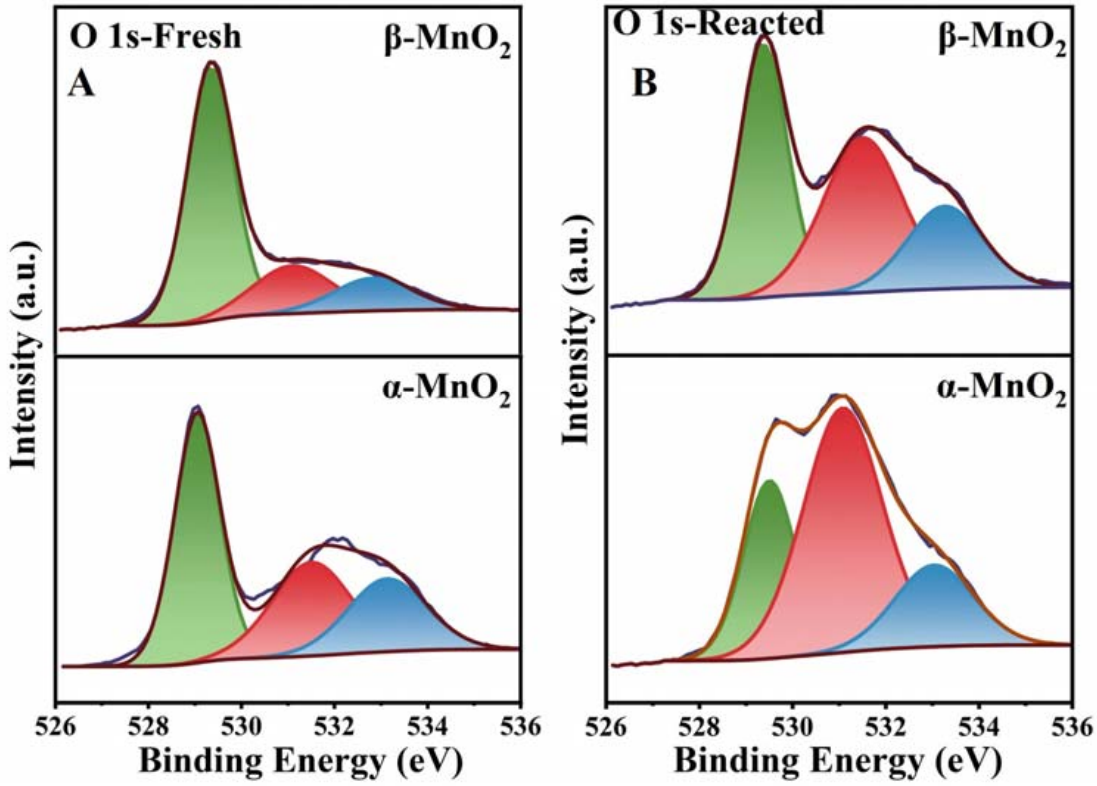

Figure 11. XPS profiles of O 1s over the fresh (**A**) and spent (**B**) catalysts.

Table 2. O 1s results before and after the reaction of B-MnO_2 and C-MnO_2.

Catalysts	O_{ads}	O_{H2O}	O_{latt}	O_{ads}/O_{latt}
α-MnO_2-Fresh	30.22	23.53	46.25	0.65
β-MnO_2-Fresh	20.68	14.10	65.22	0.32
α-MnO_2-Spent	55.20	18.39	26.41	2.09
β-MnO_2-Spent	39.78	20.34	39.87	1.00

3.5. Product Detection during the Reaction

The main gas phase products were monitored quantitatively to better understand the reaction process of CH_3SH over two different catalysts. As displayed in Figure 12, the decomposition of CH_3SH at different temperatures corresponded to the production of CH_3SSCH_3. Meanwhile, the concentration of CH_3SH during the reaction showed an excellent correlation with the concentration of CH_3SSCH_3, indicating that CH_3SSCH_3 was the main gas-phase product. At 150 °C, CH_3SH was completely decomposed for both MnO_2 catalysts, consistent with the thermodynamic theory that catalytic reactions proceed easier at higher temperatures. The yield of CH_3SSCH_3 gradually decreased when T > 100 °C, which may be due to the further catalytic oxidation of CH_3SSCH_3 at higher temperatures.

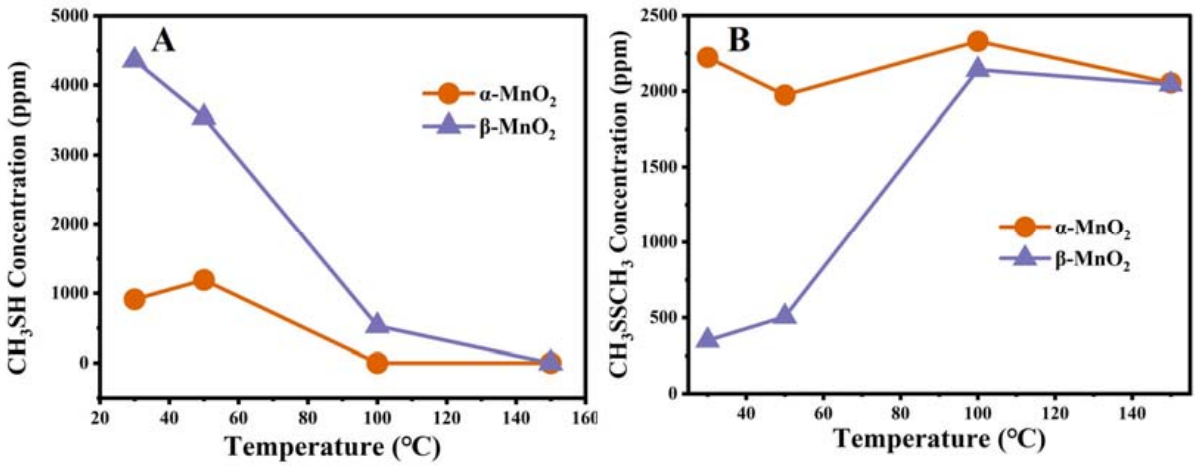

Figure 12. The CH_3SH (**A**) and CH_3SSCH_3 (**B**) concentration on α-MnO_2 and β-MnO_2.

Figure 13 shows the changes of S 2p before and after the reaction, which was used to detect the solid-phase intermediates in the reaction process. No S species were detected on two catalysts before the reaction. In contrast, significant amounts of S species were detected on both samples after the reaction, indicating that some sulfur-containing products were adsorbed on the catalyst surface. As shown in Figure 13B, three peaks at 163.2, 167.9, and 169.2 eV corresponding to S^0, SO_3^{2-} (S^{4+}), and SO_4^{2-} (S^{6+}), respectively [30,54], which all showed higher valence than S^{2-} from CH_3SH, indicating the oxidation of S during the reaction. It is worth noting that the catalytic experiments in CH_3SH were performed under a nitrogen atmosphere, so it can be concluded that the O in the S-O species was mainly derived from the O_{ads} of MnO_2. This illustrated the O_{ads} involvement in the catalytic reaction of CH_3SH. SO_3^{2-} and SO_4^{2-} were mainly retained on the manganese dioxide surface in the form of $MnSO_3$ and $MnSO_4$, implying that chemisorption was a prerequisite for the decomposition of CH_3SH on MnO_2. Notably, reacted α-MnO_2 showed a higher proportion of SO_4^{2-} (S^{6+}) (26.31%) than β-MnO_2 (12.56%) (Table 3 and Figure 13B), suggesting a greater degree of S oxidation, which corresponds to a greater reduction of Mn^{4+} after the reaction (Table 1 and Figure 9B). Furthermore, SO_4^{2-} requires more oxygen to be coordinated with S than SO_3^{2-}, so a higher proportion of SO_4^{2-} production requires more O_{ads} to participate in the reaction. Correspondingly, the H_2-TPR, O_2-TPD, and XPS analysis demonstrated more O_{ads} and better surface oxygen mobility for α-MnO_2 than β-MnO_2.

Based on the above experimental and characterization analysis, the catalytic mechanism of CH_3SH by α-MnO_2 and β-MnO_2 can be inferred in Figure 14. CH_3SH was first chemisorbed on the MnO_2 surface and subsequently underwent a single electron transfer to form $CH_3S\cdot$, and then the two $CH_3S\cdot$ were coupled to form CH_3SSCH_3. Based on the formation of S-S bonds, it is speculated that the single electron transfer occurs on S, suggesting that the chemisorption may be through the formation of Mn-S bonds. Moreover,

more lattice oxygen was released during the reduction of Mn, which was involved in the further catalytic oxidation of S-containing species to produce SO_3^{2-} and SO_4^{2-}, and may further form new oxygen vacancies to support more active sites. Although β-MnO_2 enjoys a higher AOS based on the proportion of high valence Mn, α-MnO_2 showed better catalytic activity due to more oxygen vacancies and stronger oxygen mobility.

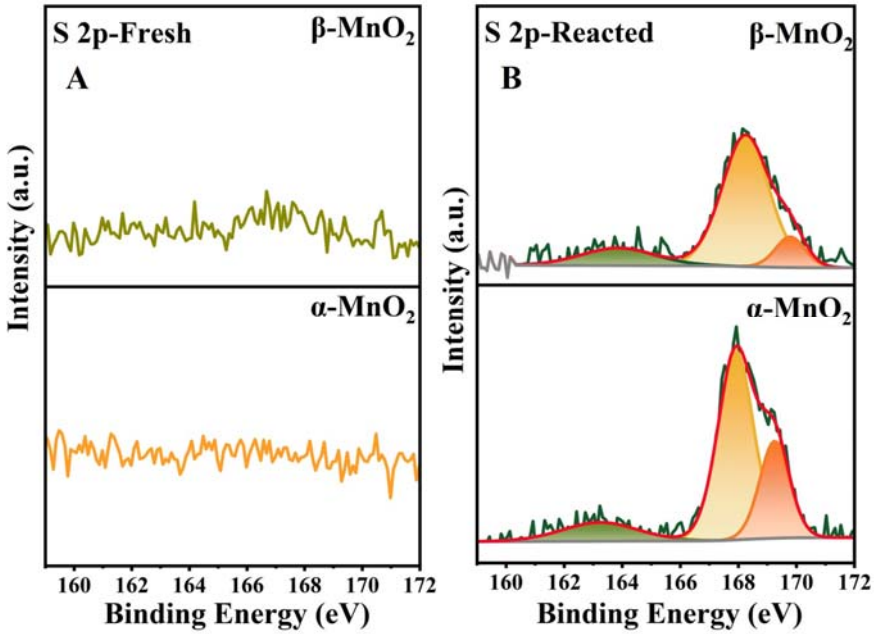

Figure 13. XPS profiles of S 2p over the fresh (**A**) and spent (**B**) catalysts.

Table 3. S 2p results before and after the reaction of B-MnO_2 and C-MnO_2.

Catalysts	S^0	S^{4+}	S^{6+}
α-MnO_2-Fresh	0	0	0
β-MnO_2-Fresh	0	0	0
α-MnO_2-Spent	12.96	60.73	26.31
β-MnO_2-Spent	13.38	74.06	12,56

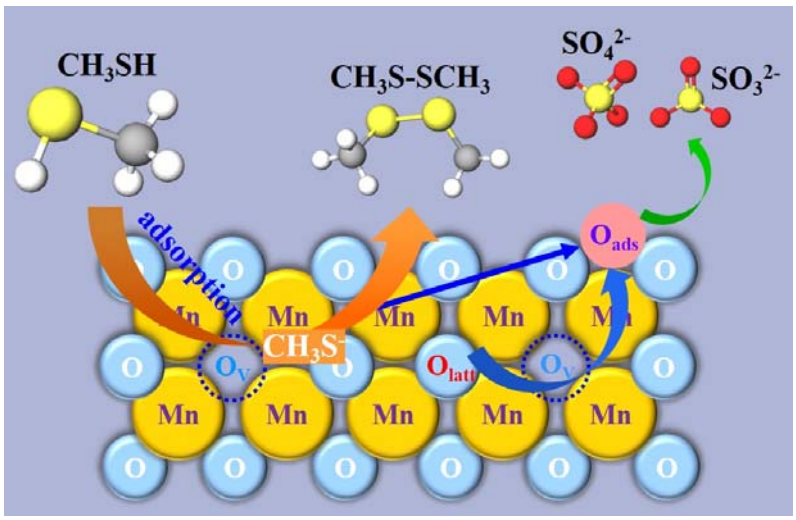

Figure 14. Reaction mechanism of CH_3SH decomposition over MnO_2 catalysts.

4. Conclusions

In this paper, MnO_2 catalysts with similar morphology but different crystal structures (α-MnO_2 and β-MnO_2) were successfully prepared, and the effects of the physicochemical properties on the catalytic activities were systematically investigated. Both Mn-based catalysts showed significant removal of CH_3SH at 150 °C, achieving complete conversion, whereas α-MnO_2 exhibited significantly better catalytic activity compared to β-MnO_2 at a lower temperature (T < 100 °C) under a GHSV of 9000 mL g^{-1} h^{-1}. Coupled with O_2-TPD, H_2-TPR, Raman spectra, XPS, EPR, and HRTEM, it was demonstrated that α-MnO_2 has more oxygen vacancies, stronger surface oxygen migration ability, and better redox properties, which can be favorable for CH_3SH decomposition. The readily released lattice oxygen during the reaction promoted further oxidative decomposition of S-containing species. The intermediate products of the solid and gas phases were determined as CH_3SSCH_3 and the S^0, SO_3^{2-}, and SO_4^{2-}, respectively. The catalytic mechanism was further proposed as the oxygen vacancies on MnO_2 provided active sites for the adsorption of CH_3SH, facilitating the electron transfer of MnO_2 with CH_3SH, and the oxygen species derived from the Mn surface were further involved in the CH_3SH catalytic oxidation. The findings of this study are essential for broadening the application of Mn-based catalysts in the removal of S-VOCs and providing new insights into the mechanism of interfacial reactions between VOCs and metal-based catalysts.

Author Contributions: Conceptualization, J.L. (Jiangping Liu) and Y.L.; data curation, H.S., J.L. (Jiangping Liu), Y.H., T.A. and Y.L.; writing—original draft preparation, H. S.; writing—review and editing, J.L. (Jiangping Liu) and J.L. (Jichang Lu); investigation: C.G. All authors have read and agreed to the published version of the manuscript.

Funding: This work was supported by National Natural Science Foundation of China (No. 42207127, 42030712, 21966018), Key Project of Natural Science Foundation of Yunnan Province (Grant No. 202101AS070026) and Applied Basic Research Foundation of Yunnan Province (Grant No. 202101BE070001-027, 2022J0069 and 202105AE160019).

Data Availability Statement: All date used to support the findings of this study are included within the article.

Conflicts of Interest: The authors declare no conflict of interest.

References

1. Guo, C.; Zhu, J.; He, J.; Hu, L.; Li, D. Catalytic oxidation/photocatalytic degradation of ethyl mercaptan on α-MnO_2@$H_4Nb_6O_{17}$-NS nanocomposite. *Vacuum* **2020**, *182*, 109718. [CrossRef]
2. Pétron, G.; Frost, G.; Miller, B.R.; Hirsch, A.I. Hydrocarbon emissions characterization in the Colorado Front Range: A pilot study. *J. Geophys. Res.* **2012**, *117*, D04304. [CrossRef]
3. He, D.; Zhao, Y.; Yang, S.; Mei, Y.; Yu, J.; Liu, J.; Chen, D.; He, S.; Luo, Y. Enhancement of catalytic performance and resistance to carbonaceous deposit of lanthanum (La) doped HZSM-5 catalysts for decomposition of methyl mercaptan. *Chem. Eng. J.* **2018**, *336*, 579–586. [CrossRef]
4. Lu, J.; Hao, H.; Zhang, L.; Xu, Z.; Zhong, L.; Zhao, Y.; He, D.; Liu, J.; Chen, D.; Pu, H.; et al. The investigation of the role of basic lanthanum (La) species on the improvement of catalytic activity and stability of HZSM-5 material for eliminating methanethiol-(CH_3SH). *Appl. Catal. B* **2018**, *237*, 185–197. [CrossRef]
5. Zhao, S.; Yi, H.; Tang, X.; Kang, D.; Gao, F.; Wang, J.; Huang, Y.; Yang, Z. Removal of volatile odorous organic compounds over NiAl mixed oxides at low temperature. *J. Hazard. Mater.* **2018**, *344*, 797. [CrossRef]
6. Yi, H.; Tao, T.; Zhao, S.; Yu, Q.; Gao, F.; Zhou, Y.; Tang, X. Promoted adsorption of methyl mercaptan by γ-Al_2O_3 catalyst loaded with Cu/Mn. *Environ. Technol. Inno.* **2021**, *21*, 101349. [CrossRef]
7. Roman, P.; Veltman, R.; Bijmans, F.M.M.; Keesman, K.J.; Janssen, A.J.H. Effect of methanethiol concentration on sulfur production in biological desulfurization systems under haloalkaline conditions. *Environ. Sci. Technol.* **2015**, *49*, 9212. [CrossRef]
8. Hu, L.; He, H.; Xia, D.; Huang, Y.; Xu, J.; Li, H.; He, C.; Yang, W.; Shu, D.; Wong, P.K. Highly Efficient Performance and Conversion Pathway of Photocatalytic CH_3SH Oxidation on Self-Stabilized Indirect Z-Scheme g-C_3N_4/I_3-BiOI. *ACS Appl. Mater. Inter.* **2018**, *10*, 18693–18708. [CrossRef]
9. He, C.; Liao, Y.; Chen, C.; Xia, D.; Wang, Y.; Tian, S.; Yang, J.; Shu, D. Realizing a redox-robust Ag/MnO_2 catalyst for efficient wet catalytic ozonation of S-VOCs: Promotional role of Ag(0)/Ag(I)-Mn based redox shuttle. *Appl. Cataly. B* **2022**, *303*, 120881. [CrossRef]

10. Lian, Q.; Hu, L.; Ma, D.; Jiao, Y.; Xia, D.; Huang, Y.; Tang, Z.; Qu, W.; Zhao, H.; He, C.; et al. Interstitial Atomic Bi Charge-Alternating Processor Boosts Twofold Molecular Oxygen Activation Enabling Rapid Catalytic Oxidation Reactions at Room Temperature. *Advan. Func. Mater.* **2022**, *32*, 2205054. [CrossRef]
11. Liu, J.; He, D.; Chen, D.; Hao, H.; Yu, J.; Lu, J.; Liu, F.; Liu, P.; Zhao, Y.; Luo, Y. Promotional effects of rare-earth (La, Ce and Pr) modification over HZSM-5 for methyl mercaptan catalytic decomposition. *J. Taiwan Ins.Chem. Eng.* **2017**, *80*, 262–268. [CrossRef]
12. Zhao, Y.; Chen, D.; Liu, J.; He, D.; Cao, X.; Han, C.; Lu, J.; Luo, Y. Tuning the metal-support interaction on chromium-based catalysts for catalytically eliminate methyl mercaptan: Anchored active chromium species through surface hydroxyl groups. *Chem. Eng. J.* **2020**, *389*, 124384. [CrossRef]
13. Tian, F.-X.; Li, H.; Zhu, M.; Tu, W.; Lin, D.; Han, Y.-F. Effect of MnO_2 Polymorphs' Structure on Low-Temperature Catalytic Oxidation: Crystalline Controlled Oxygen Vacancy Formation. *ACS Appl. Mater. Inter.* **2022**, *14*, 18525–18538. [CrossRef]
14. Huang, J.; Zhong, S.; Dai, Y.; Liu, C.-C.; Zhang, H. Effect of MnO_2 Phase Structure on the Oxidative Reactivity toward Bisphenol A Degradation. *Environ. Sci. Technol.* **2018**, *52*, 11309–11318. [CrossRef]
15. Zhang, K.; Han, X.; Hu, Z.; Zhang, X.; Tao, Z.; Chen, J. Nanostructured Mn-based oxides for electrochemical energy storage and conversion. *Chem. Soc. Rev.* **2015**, *44*, 699–728. [CrossRef]
16. Yang, R.; Fan, Y.; Ye, R.; Tang, Y.; Cao, X.; Yin, Z.; Zeng, Z. MnO_2-Based Materials for Environmental Applications. *Advan. Mater.* **2021**, *33*, 2004862. [CrossRef]
17. Wang, Y.; Liu, K.; Wu, J.; Hu, Z.; Huang, L.; Zhou, J.; Ishihara, T.; Guo, L. Unveiling the Effects of Alkali Metal Ions Intercalated in Layered MnO_2 for Formaldehyde Catalytic Oxidation. *ACS Catal.* **2020**, *10*, 10021–10031. [CrossRef]
18. Sun, W.; Kitchaev, D.A.; Kramer, D.; Ceder, G. Non-equilibrium crystallization pathways of manganese oxides in aqueous solution. *Nat. Commun.* **2019**, *10*, 573. [CrossRef]
19. Hayashi, E.; Yamaguchi, Y.; Kamata, K.; Tsunoda, N.; Kumagai, Y.; Oba, F.; Hara, M. Effect of MnO_2 Crystal Structure on Aerobic Oxidation of 5-Hydroxymethylfurfural to 2,5-Furandicarboxylic Acid. *Jo. Amer. Chem. Soc.* **2019**, *141*, 890–900. [CrossRef]
20. Chen, B.; Wu, B.; Yu, L.; Crocker, M.; Shi, C. Investigation into the Catalytic Roles of Various Oxygen Species over Different Crystal Phases of MnO_2 for C_6H_6 and HCHO Oxidation. *ACS Catal.* **2020**, *10*, 6176–6187. [CrossRef]
21. Shi, J.; Qi, T.; Sun, B.C.; Chu, G.W.; Chen, J.F. Catalytic oxidation of benzyl alcohol over MnO_2: Structure-activity description and reaction mechanism. *Chem. Eng. J.* **2022**, *440*, 135802. [CrossRef]
22. Jiao, F.; Bruce, P.G. Mesoporous Crystalline β-MnO_2-a Reversible Positive Electrode for Rechargeable Lithium Batteries. *Advan. Mater.* **2007**, *19*, 657–660. [CrossRef]
23. Hayashi, E.; Yamaguchi, Y.; Kita, Y.; Kamata, K.; Hara, M. One-pot aerobic oxidative sulfonamidation of aromatic thiols with ammonia by a dual-functional β-MnO_2 nanocatalyst. *Chem. Commun.* **2020**, *56*, 2095–2098. [CrossRef] [PubMed]
24. Li, H.; Shang, H.; Li, Y.; Cao, X.; Yang, Z.; Ai, Z.; Zhang, L. Interfacial Charging–Decharging Strategy for Efficient and Selective Aerobic NO Oxidation on Oxygen Vacancy. *Environ. Sci. Technol.* **2019**, *53*, 6964–6971. [CrossRef]
25. Rong, S.; Zhang, P.; Liu, F.; Yang, Y. Engineering Crystal Facet of α-MnO_2 Nanowire for Highly Efficient Catalytic Oxidation of Carcinogenic Airborne Formaldehyde. *ACS Catal.* **2018**, *8*, 3435–3446. [CrossRef]
26. Wang, Y.; Liu, M.; Hu, C.; Xin, Y.; Ma, D.; Gao, M.; Xie, H. Enhanced MnO_2/peroxymonosulfate activation for phthalic acid esters degradation: Regulation of oxygen vacancy. *Chem. Eng. J.* **2022**, *433*, 134048. [CrossRef]
27. Yang, R.; Guo, Z.; Cai, L.; Zhu, R.; Fan, Y.; Zhang, Y.; Han, P.; Zhang, W.; Zhu, X.; Zhao, Q.; et al. Investigation into the Phase-Activity Relationship of MnO_2 Nanomaterials toward Ozone-Assisted Catalytic Oxidation of Toluene. *Small* **2021**, *17*, 2103052. [CrossRef]
28. Yang, W.; Su, Z.A.; Xu, Z.; Yang, W.; Peng, Y.; Li, J. Comparative study of α-, β-, γ- and δ-MnO_2 on toluene oxidation: Oxygen vacancies and reaction intermediates. *Appl. Catal. B* **2020**, *260*, 118150. [CrossRef]
29. Zhao, Z.; Li, G.; Sun, Y.; Li, N.; Zhang, Z.; Cheng, J.; Ma, C.; Hao, Z. The positive effect of water on acetaldehyde oxidation depended on the reaction temperature and MnO_2 structure. *Appl. Catal. B* **2022**, *303*, 120886. [CrossRef]
30. Zheng, X.; Zhang, G.; Yao, Z.; Zheng, Y.; Shen, L.; Liu, F.; Cao, Y.; Liang, S.; Xiao, Y.; Jiang, L. Engineering of crystal phase over porous MnO_2 with 3D morphology for highly efficient elimination of H_2S. *J. Hazard. Mater.* **2021**, *411*, 125180. [CrossRef]
31. Zhu, G.; Zhu, J.; Jiang, W.; Zhang, Z.; Wang, J.; Zhu, Y.; Zhang, Q. Surface oxygen vacancy induced α-MnO_2 nanofiber for highly efficient ozone elimination. *Appl. Catal. B* **2017**, *209*, 729–737. [CrossRef]
32. Huang, N.; Qu, Z.; Dong, C.; Qin, Y.; Duan, X. Superior performance of α@β-MnO_2 for the toluene oxidation: Active interface and oxygen vacancy. *Appl. Catal. A* **2018**, *560*, 195–205. [CrossRef]
33. Yu, D.; Wang, L.; Zhang, C.; Peng, C.; Yu, X.; Fan, X.; Liu, B.; Li, K.; Li, Z.; Wei, Y.; et al. Alkali Metals and Cerium-Modified La-Co-Based Perovskite Catalysts: Facile Synthesis, Excellent Catalytic Performance, and Reaction Mechanisms for Soot Combustion. *ACS Catal.* **2022**, *12*, 15056–15075. [CrossRef]
34. Guan, S.; Huang, Q.; Ma, J.; Li, W.; Ogunbiyi, A.T.; Zhou, Z.; Chen, K.; Zhang, Q. HCHO Removal by MnO_2(x)-CeO_2: Influence of the Synergistic Effect on the Catalytic Activity. *Ind. Eng. Chem. R.* **2020**, *59*, 596–608. [CrossRef]
35. Chen, L.; Zhang, C.; Li, Y.; Chang, C.-R.; He, C.; Lu, Q.; Yu, Y.; Duan, P.; Zhang, Z.; Luque, R. Hierarchically Hollow MnO_2@CeO_2 Heterostructures for NO Oxidation: Remarkably Promoted Activity and SO_2 Tolerance. *ACS Catal.* **2021**, *11*, 10988–10996. [CrossRef]
36. Zheng, C.; Bao, S.; Mao, D.; Xu, Z.; Zheng, S. Insight into phase structure-dependent soot oxidation activity of K/MnO2 catalyst. *J. Environ. Sci.* **2023**, *126*, 668–682. [CrossRef]

37. Wu, S.; Liu, H.; Huang, Z.; Xu, H.; Shen, W. O-vacancy-rich porous MnO_2 nanosheets as highly efficient catalysts for propane catalytic oxidation. *Appl. Catal. B* **2022**, *312*, 121387. [CrossRef]
38. Wan, J.; Zhou, L.; Deng, H.; Zhan, F.; Zhang, R. Oxidative degradation of sulfamethoxazole by different MnO_2 nanocrystals in aqueous solution. *J. Molecular Catal. A* **2015**, *407*, 67–74. [CrossRef]
39. Cheng, S.; Yang, L.; Chen, D.; Ji, X.; Jiang, Z.; Ding, D.; Liu, M. Phase evolution of an alpha MnO_2-based electrode for pseudo-capacitors probed by in operando Raman spectroscopy. *Nano Energy* **2014**, *9*, 161–167. [CrossRef]
40. Shan, C.; Zhang, Y.; Zhao, Q.; Fu, K.; Zheng, Y.; Han, R.; Liu, C.; Ji, N.; Wang, W.; Liu, Q. Acid Etching-Induced In Situ Growth of λ-MnO_2 over CoMn Spinel for Low-Temperature Volatile Organic Compound Oxidation. *Environ. Sci. Technol.* **2022**, *56*, 10381–10390. [CrossRef]
41. Chen, G.; Hong, D.; Xia, H.; Sun, W.; Shao, S.; Gong, B.; Wang, S.; Wu, J.; Wang, X.; Dai, Q. Amorphous and homogeneously Zr-doped MnOx with enhanced acid and redox properties for catalytic oxidation of 1,2-Dichloroethane. *Chem. Eng. J.* **2022**, *428*, 131067. [CrossRef]
42. Wei, Y.J.; Yan, L.Y.; Wang, C.Z.; Xu, X.G.; Wu, F.; Chen, G. Effects of Ni Doping on [MnO_6] Octahedron in $LiMn_2O_4$. *J. Phy. Chem. B* **2004**, *108*, 18547–18551. [CrossRef]
43. Zhang, S.; Wang, H.; Si, H.; Jia, X.; Wang, Z.; Li, Q.; Kong, J.; Zhang, J. Novel Core–Shell (ε-MnO_2/CeO_2)@CeO_2 Composite Catalyst with a Synergistic Effect for Efficient Formaldehyde Oxidation. *ACS Appl. Mater. Inter.* **2020**, *12*, 40285–40295. [CrossRef] [PubMed]
44. Wu, P.; Dai, S.; Chen, G.; Zhao, S.; Xu, Z.; Fu, M.; Chen, P.; Chen, Q.; Jin, X.; Qiu, Y.; et al. Interfacial effects in hierarchically porous α-MnO_2/Mn_3O_4 heterostructures promote photocatalytic oxidation activity. *Appl. Catal. B* **2020**, *268*, 118418. [CrossRef]
45. Nawaz, F.; Cao, H.; Xie, Y.; Xiao, J.; Chen, Y.; Ghazi, Z.A. Selection of active phase of MnO_2 for catalytic ozonation of 4-nitrophenol. *Chemosphere* **2017**, *168*, 1457–1466. [CrossRef] [PubMed]
46. Ding, D.; Zhou, Y.; He, T.; Rong, S. Facet selectively exposed α-MnO_2 for complete photocatalytic oxidation of carcinogenic HCHO at ambient temperature. *Chem. Eng. J.* **2022**, *431*, 133737. [CrossRef]
47. Jia, J.; Zhang, P.; Chen, L. Catalytic decomposition of gaseous ozone over manganese dioxides with different crystal structures. *Appl. Catal. B* **2016**, *189*, 210–218. [CrossRef]
48. Zhang, Y. Electronegativities of elements in valence states and their applications. 1. Electronegativities of elements in valence states. *Inorg. Chem.* **1982**, *21*, 3886–3889. [CrossRef]
49. Liu, J.; Wang, H.; Wang, L.; Jian, P.; Yan, X. Phase-dependent catalytic performance of MnO_2 for solvent-free oxidation of ethybenzene with molecular oxygen. *Appl. Catal. B* **2022**, *305*, 121050. [CrossRef]
50. Wang, J.; Cheng, L.; An, W.; Xu, J.; Men, Y. Boosting soot combustion efficiencies over CuO-CeO_2 catalysts with a 3DOM structure. *Catal. Sci. Technol.* **2016**, *6*, 7342–7350. [CrossRef]
51. Liu, J.; Meng, R.; Li, J.; Jian, P.; Wang, L.; Jian, R. Achieving high-performance for catalytic epoxidation of styrene with uniform magnetically separable $CoFe_2O_4$ nanoparticles. *Appl. Catal. B* **2019**, *254*, 214–222. [CrossRef]
52. He, T.; Shao, D.; Zeng, X.; Rong, S. Harvesting the vibration energy of α-MnO_2 nanostructures for complete catalytic oxidation of carcinogenic airborne formaldehyde at ambient temperature. *Chemosphere* **2020**, *261*, 127778. [CrossRef] [PubMed]
53. Setvín, M.; Aschauer, U.; Scheiber, P.; Li, Y.F.; Hou, W.; Schmid, M.; Selloni, A.; Diebold, U. Reaction of O_2 with Subsurface Oxygen Vacancies on TiO_2 Anatase (101). *Science* **2013**, *341*, 988–991. [CrossRef] [PubMed]
54. Cao, X.; Lu, J.; Zheng, X.; He, D.; Zhu, W.; Zhao, Y.; Zhang, W.; Tian, R.; Luo, Y. Regulation of the reaction pathway to design the high sulfur/coke-tolerant Ce-based catalysts for decomposing sulfur-containing VOCs. *Chem. Eng. J.* **2022**, *429*, 132473. [CrossRef]